DOT/FAA/AR-08/48

Air Traffic Organization
Operations Planning
Office of Aviation Research
and Development
Washington, DC 20591

Impact and Delamination Failure Characterization of BMS 8-212 Composite Aircraft Material

October 2008

Final Report

This document is available to the U.S. public through the National Technical Information Services (NTIS), Springfield, Virginia 22161.

U.S. Department of Transportation
Federal Aviation Administration

NOTICE

This document is disseminated under the sponsorship of the U.S. Department of Transportation in the interest of information exchange. The United States Government assumes no liability for the contents or use thereof. The United States Government does not endorse products or manufacturers. Trade or manufacturer's names appear herein solely because they are considered essential to the objective of this report. This document does not constitute FAA certification policy. Consult your local FAA aircraft certification office as to its use.

This report is available at the Federal Aviation Administration William J. Hughes Technical Center's Full-Text Technical Reports page: actlibrary.tc.faa.gov in Adobe Acrobat portable document format (PDF).

Technical Report Documentation Page

1. Report No.	2. Government Accession No.	3. Recipient's Catalog No.
DOT/FAA/AR-08/48		

4. Title and Subtitle	5. Report Date
IMPACT AND DELAMINATION FAILURE CHARACTERIZATION OF BMS 8-212 COMPOSITE AIRCRAFT MATERIAL	October 2008
	6. Performing Organization Code
7. Author(s) David Powell, Tarek Zohdi, and George Johnson	8. Performing Organization Report No.
9. Performing Organization Name and Address University of California, Berkeley Mechanical Engineering Department 6117 Etcheverry Hall Berkeley, CA 94720-1740	10. Work Unit No. (TRAIS)
	11. Contract or Grant No. 01-C-AW-UCB
12. Sponsoring Agency Name and Address U.S. Department of Transportation Federal Aviation Administration Air Traffic Organization Operations Planning Office of Aviation Research and Development Washington, DC 20591	13. Type of Report and Period Covered Final Report 1/2005 – 12/2007
	14. Sponsoring Agency Code ANM-100

15. Supplementary Notes

The Federal Aviation Administration Airport and Aircraft Safety R&D Division Technical Monitor was Donald Altobelli.

16. Abstract

This study was part of a program, sponsored by the Federal Aviation Administration that focused on understanding the behavior of different aircraft materials under impact in the speed range generated from engine uncontained failures. This test program investigated the material response of 8-, 16-, and 32-ply BMS8-212 composite panels provided by The Boeing Company. All tests were performed at the University of California, Berkeley ballistics laboratory using a pneumatic gas gun and half-inch-diameter spherical and flat-ended cylindrical projectiles. The ballistic impact tests indicated that the amount of energy absorbed by a similar composite target panel during impacts above the ballistic limit was nearly constant, showing only a slight increase with increasing initial energy. The amount of energy absorbed per ply increased only slightly for thicker panels. The tests also showed that the cylindrical projectiles required more energy to penetrate the composite panels than the spherical projectiles.

17. Key Words	18. Distribution Statement
Composite, Testing, Aircraft, Impact, Fragments, Containment, Ballistics	This document is available to the U.S. public through the National Technical Information Service (NTIS), Springfield, Virginia 22161.

19. Security Classif. (of this report)	20. Security Classif. (of this page)	21. No. of Pages	22. Price
Unclassified	Unclassified	40	

Form DOT F 1700.7 (8-72) Reproduction of completed page authorized

TABLE OF CONTENTS

		Page
EXECUTIVE SUMMARY		vii
1.	INTRODUCTION	1
2.	EXPERIMENTAL SETUP	1
2.1	Initial Velocity Measurement	2
2.2	Target Holder and Mount	3
2.3	Residual Velocity Measurement	3
3.	EXPERIMENTAL PROCEDURE	4
4.	EXPERIMENTAL RESULTS AND DISCUSSION	5
4.1	Projectiles	5
4.2	Composite Material	5
4.3	Test Results and Discussion	5
4.3.1	Ballistic Curves	5
4.3.2	Energy Absorbed	7
4.3.3	Composite Test Data	10
4.3.4	Damage Characterization	13
4.3.5	Composite During Impact	14
5.	ERROR ANALYSIS	15
5.1	Initial Velocity	15
5.2	Residual Velocity	16
5.3	Delamination Testing	18
6.	SUMMARY	18
7.	REFERENCES	19
APPENDICES		
	A—BMS 8-212 Properties	
	B—BMS 8-212 Delamination Testing Results	

LIST OF FIGURES

Figure		Page
1	Pneumatic Gas Gun Setup Used in the Experiments	2
2	Initial Velocity Measurement System	2
3	Target Mount and Holder Prepared for a Test	3
4	Ballistic Response for Spherical Projectiles	6
5	Ballistic Response for Cylindrical Projectiles	7
6	Energy Absorbed During the Impact of Spherical Projectiles	8
7	Energy Absorbed During the Impact of Cylindrical Projectiles	8
8	Energy Absorbed per Ply for Spherical Projectiles	9
9	Energy Absorbed per Ply for Cylindrical Projectiles	10
10	Damage in Composite Panel Caused by Cylindrical Projectile	13
11	Damage in Composite Panel Caused by Spherical Projectile	14
12	Cylinder Impacting Composite Panel	14
13	Sphere Impacting Composite Panel	15

LIST OF TABLES

Table		Page
1	Data for 8-Ply Composite Panels	11
2	Data for 16-Ply Composite Panels	12
3	Data for 32-Ply Composite Panels	12
4	Energy Absorbed During Impact	18
5	Summary of Ballistic Limit Values	18

LIST OF SYMBOLS AND ACRONYMS

C	Conversion Factor
d	Distance
t	Time
v	Velocity
x	Distance in Pixels
FAA	Federal Aviation Administration
LLNL	Lawrence Livermore National Laboratory
UCB	University of California, Berkeley

EXECUTIVE SUMMARY

This report details the response of composite material BMS 8-212 under ballistic impact testing. Composite panels of 8, 16, and 32 plies were tested. All tests were performed at the University of California, Berkeley, ballistics laboratory using a pneumatic gas gun and half-inch-diameter spherical and flat-ended cylindrical projectiles. The ballistic impact tests showed that the amount of energy absorbed by a similar composite target panel during impact is nearly constant above the ballistic limit, showing only a slight increase with increasing initial energy. The amount of energy absorbed per ply increased only slightly for the thicker samples. The tests also showed that the cylindrical projectiles required more energy to penetrate the composite panels than the spherical projectiles.

1. INTRODUCTION.

Over the past several years, the University of California, Berkeley (UCB), sponsored by the Federal Aviation Administration (FAA) Aircraft Catastrophic Failure Prevention Program, has participated with the FAA, The Boeing Company, and Lawrence Livermore National Laboratory (LLNL) in research directed at enhancing the safety of commercial aircraft in the case of uncontained engine failure. Part of this program focused on characterizing the response of certain aircraft material to ballistic impact. Boeing provided composite material BMS 8-212 for this study. This material has been used for many years and was selected because its material properties have been publicly released.

The purpose of this study was to provide comprehensive ballistic test data for BMS 8-212. In the ballistic tests, 12- by 12-inch composite panels of varying thickness were supported at the edges and impacted by either a 0.5-inch-diameter steel ball, or cylinder, shot at various velocities to establish a ballistic limit. The projectile impact and exit (postimpact) speeds were recorded.

2. EXPERIMENTAL SETUP.

All experiments were performed using a pneumatic gas gun. The setup included an initial velocity measurement system, target holder, target mount, and a high-speed camera for residual velocity measurement. The setup was similar to previous tests conducted at UCB on fabric and metal materials [1 and 2].

The pneumatic gun used industrial-grade compressed nitrogen with a maximum pressure of 1500 psi. The pneumatic gun had a 0.5-inch-diameter barrel that was approximately 52 inches long. Starting at about 39 inches, slits were placed in the barrel that relieved the pressure behind the projectile. A regulator controlling the pressure could be set for any value between 25 and 1500 psi. The solenoid valve that releases the pressure was controlled by an electronic control box and triggered from an adjacent room. Figure 1 shows the test setup.

Figure 1. Pneumatic Gas Gun Setup Used in the Experiments

2.1 INITIAL VELOCITY MEASUREMENT.

To measure the initial velocity of the projectile, a laser/photodiode was used. Two Uniphase, helium-neon, gas laser beams were focused through the path of the projectile at two Sharp IS489 high-sensitivity light detectors placed 2.5 inches apart. As the projectile crossed the path of each laser beam, the voltage drop in the respective photodiode was detected by a Hewlett Packard 53131A Universal Counter. The distance between the detectors, 2.5 inches, was divided by the time recorded to determine the initial velocity of the projectile, as shown in figure 2.

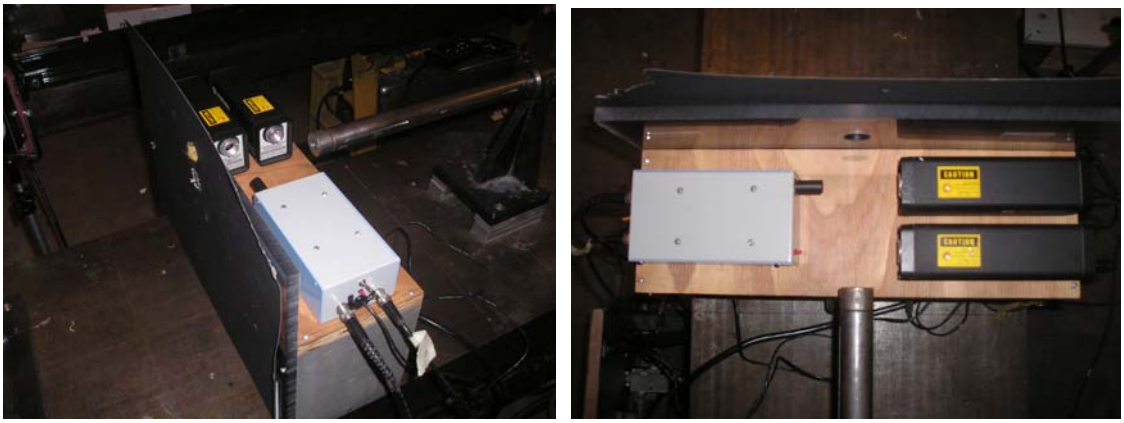

Figure 2. Initial Velocity Measurement System (Perspective and Top Views)

2.2 TARGET HOLDER AND MOUNT.

The composite target panels were placed between two half-inch-thick square steel frames. The frames were 10 inches square on the inside and 14 inches square on the outside. With the target in the middle, the two frames were held together using four 3/8-16 by 2 1/2-inch socket head cap screw (SHCS) alloy steel bolts. The bolts were hand tightened with care not to damage the composite panel.

The target holder was held in the line of the projectile by a large steel angle manufactured specifically for this purpose. The mount was made in such a way that the target holder could be positioned so any point on the 10-inch-square area could be impacted. For this study, the holder was positioned so the projectile would impact the panel in the center. Marks were placed on the target mount so the holder could be placed in exactly the same position and orientation for each shot. The target holder was held in place by four C-clamps, one placed at each corner. Figure 3 shows photographs of the target mount and holder.

Figure 3. Target Mount and Holder Prepared for a Test

2.3 RESIDUAL VELOCITY MEASUREMENT.

To measure the residual velocity, high-speed video of the impact was recorded. For the majority of the tests, a Photron Fastcam high-speed camera controller with a Kodak Motion Corder Analyzer, Series SR camera was used to capture and analyze the video. The camera was set to record the impact at 10,000 frames per second. The high-speed video used a shutter speed of 1/20,000 seconds, thus requiring a significant amount of light. For this reason, two high-intensity 650-Watt lamps were used during filming. The camera was placed approximately 9 feet away from the target mount and, due to space restrictions, a mirror was used so the camera could view and record the impact simultaneously. With a wide-angle lens, the field of view of about 10 inches wide by 2 inches high was attained. The setup was such that the majority of the view, 8 inches, was devoted to after the impact, and the remaining 2 inches showed the area prior to the impact. This was done to provide a backup in case the initial velocity measurement system malfunctioned.

For each series of shots, a scale was placed in the path of the projectile to determine how many pixels per inch the camera recorded. The camera controller allowed the user to scroll through

the pixels in the x and y directions and record the position. To measure the residual velocity of the projectile, the position of the back edge of the projectile was recorded at the moment it left the composite panel, and the time was noted. The video was stepped through until the final frame that still contained the projectile in the field of view was found. Again, the position of the back edge was recorded, as well as the time. The distance in pixels was converted into inches and then divided by the time between images to produce the velocity of the projectile.

For later tests, the system was upgraded and replaced by a Vision Research Phantom v4 Series camera. A frame rate of 10,000 frames per second was used with a shutter speed of 20,000 microseconds. The resolution was increased to 256 by 64 pixels, thus reducing the error in the measurement of the residual velocity. This camera was placed approximately 3 feet away from the target mount and filmed the impact directly. The calculation for the velocity remained unchanged.

In addition, the high-speed video provided valuable information about the composite and projectile behavior during and after impact. The files were examined to obtain any information on the failure characteristics or projectile flight behavior that might be relevant. Any abnormalities in the impact were noted and the recordings of each test were saved as Audio Video Interleave (.avi) files for later reference.

3. EXPERIMENTAL PROCEDURE.

The following test procedure was used for each of the pneumatic gun tests:

1. Targets were placed in the holder and a steel bolt was placed at each corner of the holder. The bolts were tightened by hand to hold the panel firmly in place but not tight enough to damage the panel.

2. The target holder was put into position on the target mount with the center lined up with the path of the projectile. The holder was lined up with marks drawn on the mount to ensure consistency between the shots and correct alignment of the target. Spacers were put in place so the face of the panel was perpendicular to the path of the projectile, reducing the chances of an oblique impact. The holder was then secured in place with a C-clamp at each corner.

3. The initial velocity measurement system was prepared and tested.

4. The camera was aimed and calibrated. The trigger was set to record-ready and automatically recorded when set off by the firing of the gun.

5. The pressure was set at the desired value using the regulator valve at the end of the nitrogen tank. The pressure value was chosen based on the type of projectile and the desired initial velocity.

6. The breech of the gun was slid back, and the projectile was placed into the barrel. The breech was returned to its initial position and secured in place.

7. The camera lights were turned on.

8. The room was evacuated.

9. The trigger outside the room was pressed, setting off the gun and the camera.

10. After the test, all the measurements were recorded, the velocities were calculated, and all the data was stored. The composite panel was removed, labeled, and saved for later inspection.

4. EXPERIMENTAL RESULTS AND DISCUSSION.

4.1 PROJECTILES.

Two different types of steel projectiles were used in the composite panel tests, spherical and flat-ended cylindrical projectiles. The 52100 steel spheres were one-half inch in diameter and weighed 0.018 pound (8.3 grams). The tool steel cylinders had a diameter of one-half inch, a length of 2 inches, and weighed 0.082 pound (37.1 grams).

4.2 COMPOSITE MATERIAL.

The composite material was provided by Boeing and identified as BMS 8-212. This material is a carbon fiber composite panel; however, specific details on the material makeup of the fibers and the resin were not provided. The material's density is 0.056 pounds per cubic inch. The resin content is 37% by weight. The thickness of a single cured ply is 0.0080 inches and the width of the square panel is 1 foot. The ply orientation was successively 0, 45, 90, -45, etc., degrees. This sequence was mirrored about the center plane, so two 0-degree plies would be at the center. Three different thicknesses were tested: 8, 16, and 32 plies. The Young's Modulus for a single ply in the fiber direction is 17.1 GPa and perpendicular to the fiber direction is 1.28 GPa. The shear modulus (in the 1-2, 1-3, and 2-3 directions) is 0.66 GPa. The material's Poisson's ratio is 0.34. Additional information on BMS 8-212 is shown in appendix A.

4.3 TEST RESULTS AND DISCUSSION.

4.3.1 Ballistic Curves.

The ballistic curves for the composite material are depicted in figures 4 and 5. Tables 1-3 in section 4.3.3 include the actual initial and residual velocities from the test data that are included in figures 4 and 5. Figure 4 depicts the response of the composite when impacted by lightweight spherical projectiles and figure 5 shows the response for impact by the heavier cylindrical projectiles. The ballistic limit, the highest speed at which penetration does not occur, is shown in the figures. As expected, the ballistic limit increases as the number of plies increases. The cylinders penetrate the composite panels at lower velocities, but since their weight is over four times that of the spheres, this is a little misleading. To get a better idea of the impact the

projectile shape had on the response, the energy absorbed by the composite panels was also examined.

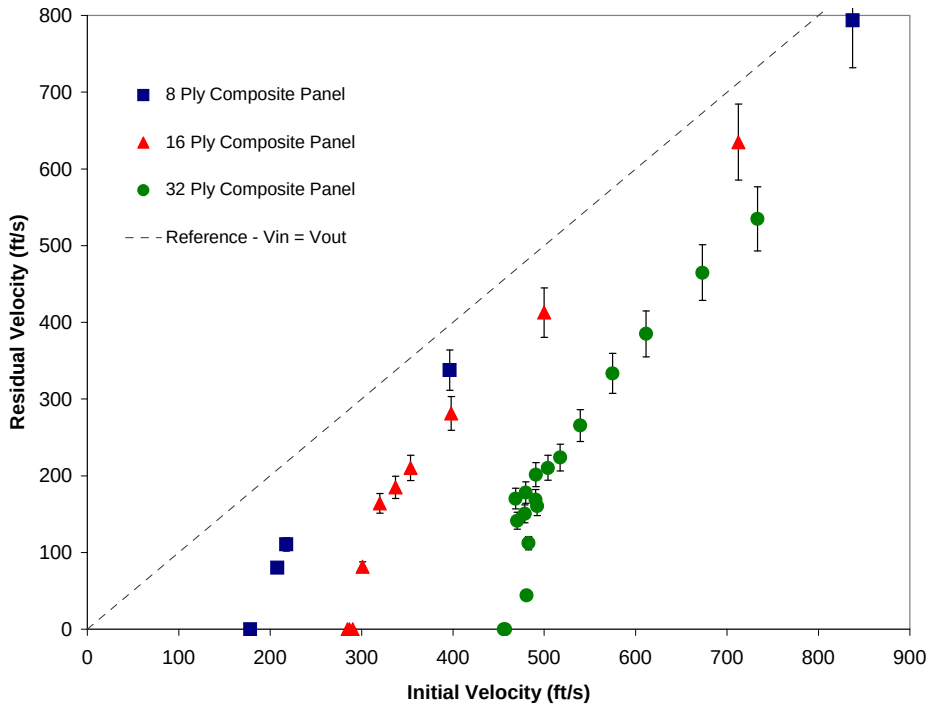

Figure 4. Ballistic Response for Spherical Projectiles

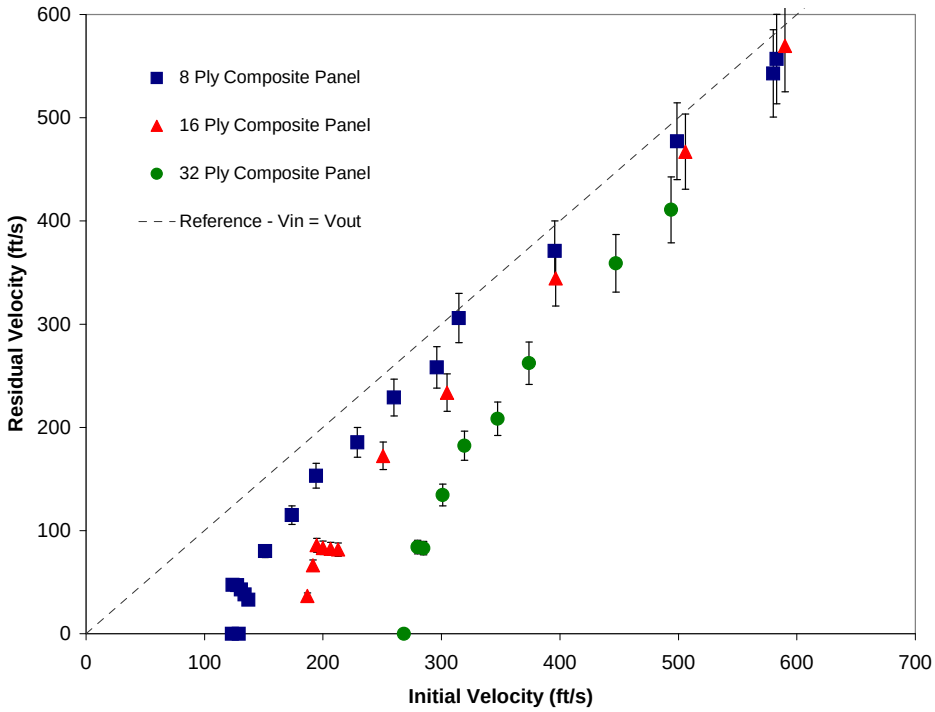

Figure 5. Ballistic Response for Cylindrical Projectiles

4.3.2 Energy Absorbed.

Figures 6 and 7 show the energy absorbed during the impact of spherical and cylindrical projectiles, respectively. While there is a slight increase in the energy absorbed as the initial energy increases, the absorbed energy remains mainly the same over the range of initial velocities. Thus, for this study, it was assumed the energy absorbed was nearly a constant above the ballistic limit. Comparing the impact of spherical projectiles with the cylindrical projectiles, it was clear that the cylindrical projectiles required more energy to penetrate the composite panels. In fact, the cylinders required almost twice the energy to penetrate the composite. During impact, the matrix of the composite cracked and the fibers separated. The shape of the spheres allowed them to push their way through the material. The cylinders, on the other hand, have a flat face that is not suited to pushing apart the fibers. Thus, the cylindrical projectiles needed to do more damage to the composite to penetrate the panel, and therefore, absorbed more energy.

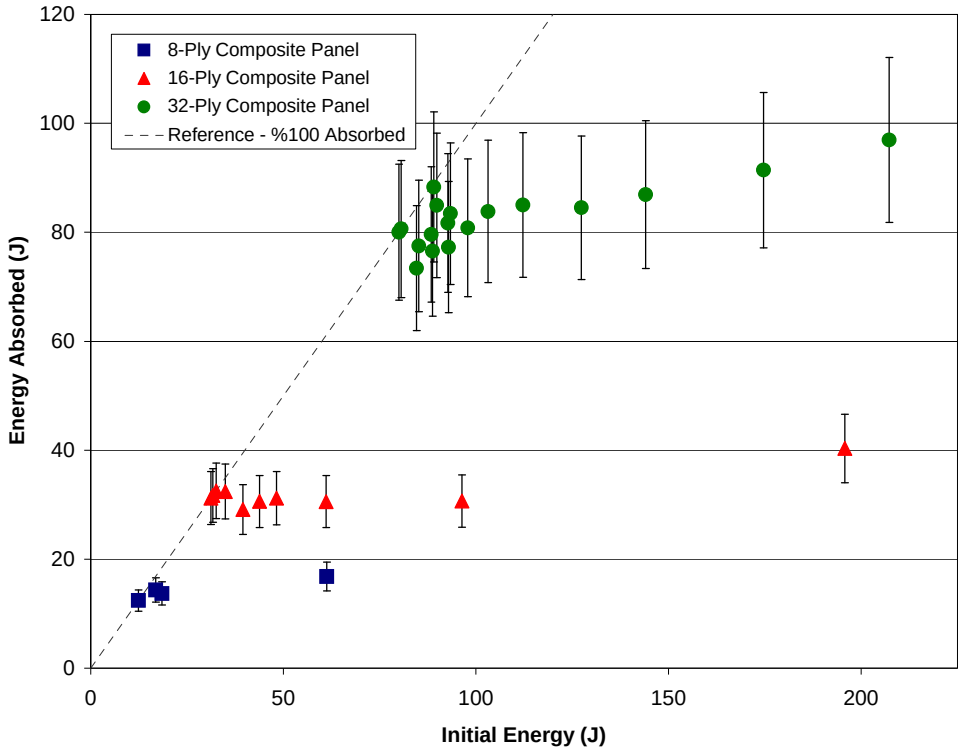

Figure 6. Energy Absorbed During the Impact of Spherical Projectiles

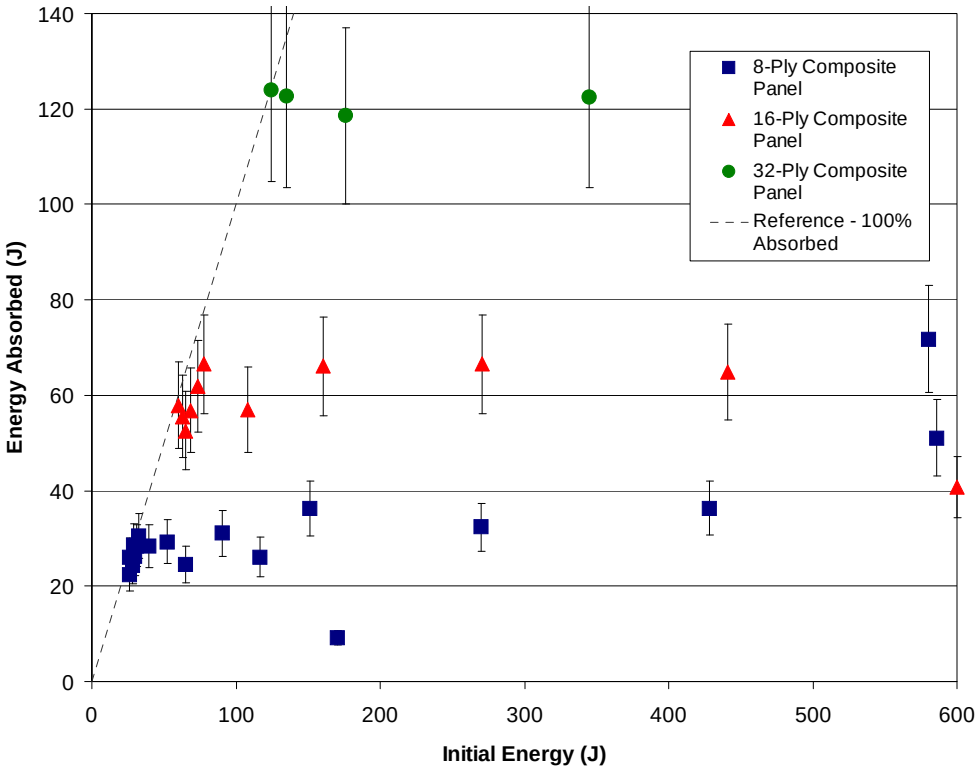

Figure 7. Energy Absorbed During the Impact of Cylindrical Projectiles

Figures 8 and 9 show the energy absorbed per ply for impact by spherical and cylindrical projectiles. For spherical projectiles, shown in figure 8, a clear increase in the energy per ply is apparent as the number of plies is increased. For the cylinders, shown in figure 9, the trend is not as clear. There appears to be a slight increase in the absorbed energy as the number of plies is increased, but the scatter of the data makes a clear determination impossible.

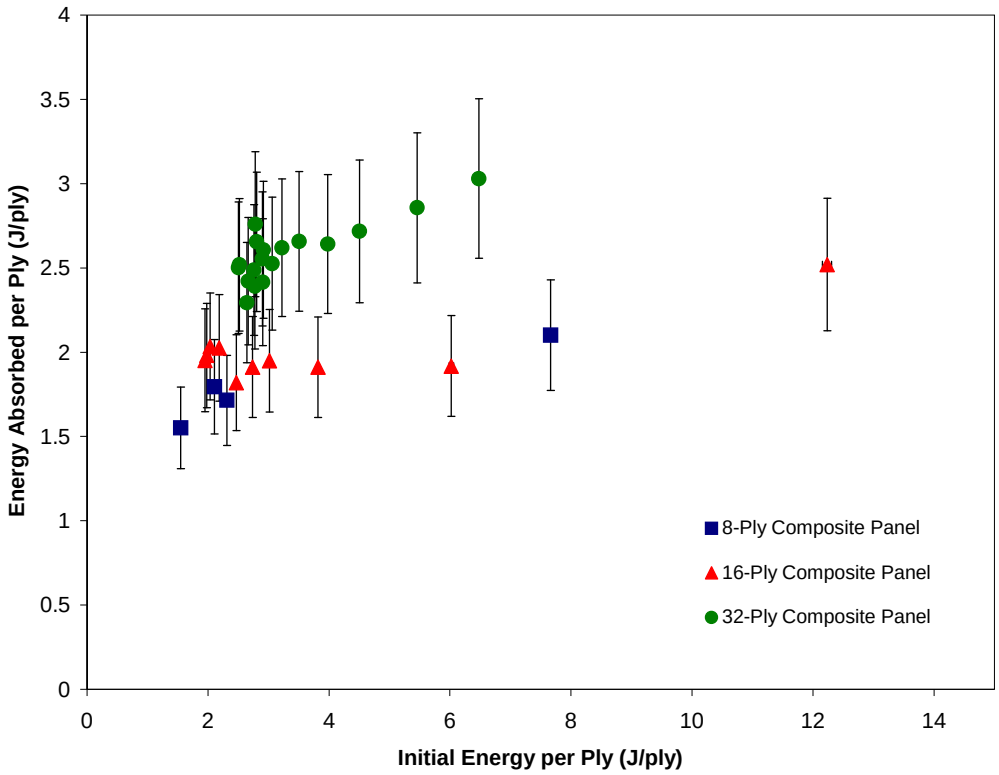

Figure 8. Energy Absorbed per Ply for Spherical Projectiles

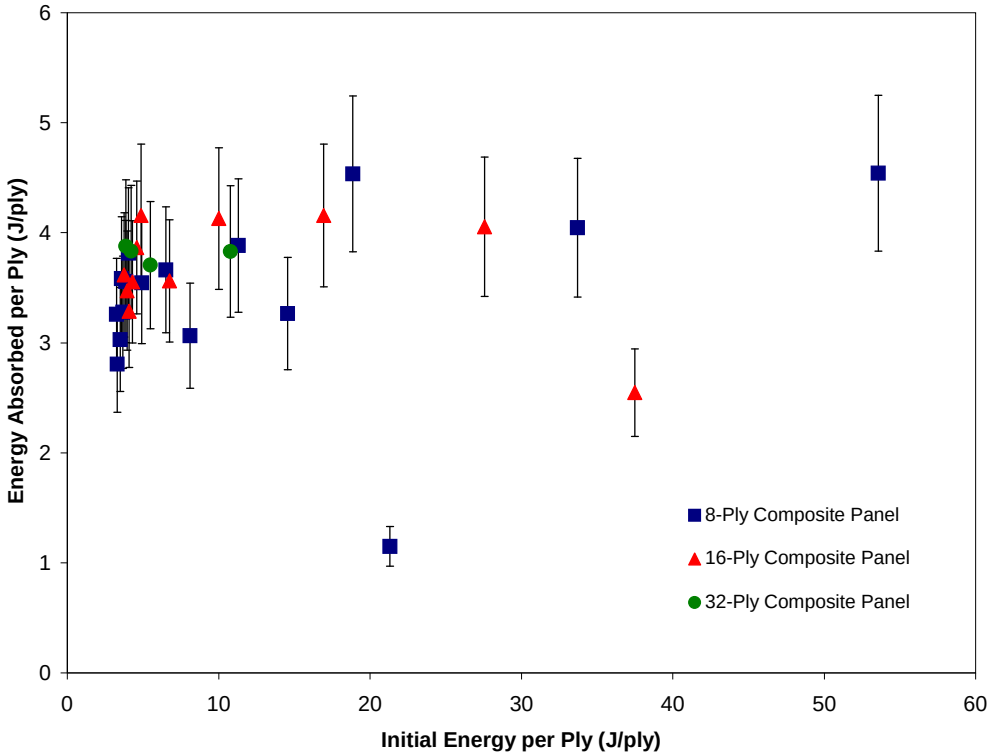

Figure 9. Energy Absorbed per Ply for Cylindrical Projectiles

4.3.3 Composite Test Data.

Tables 1 through 3 include the initial and residual velocities from the 8-, 16-, and 23-ply composite tests, respectively.

Table 1. Data for 8-Ply Composite Panels

8-Ply Cylindrical Projectile	
Initial Velocity (ft/s)	Residual Velocity (ft/s)
837.2	793.7
583.0	557.0
580.1	543.0
498.7	477.1
395.6	371.1
314.6	306.0
296.0	258.0
260.0	229.0
229.0	185.5
194.0	153.0
173.8	114.9
151.2	80.0
137.1	33.0
134.0	38.0
130.6	42.9
129.0	0.0
127.6	47.1
123.6	47.4
123.0	0.0

8-Ply Spherical Projectile	
Initial Velocity (ft/s)	Residual Velocity (ft/s)
837.2	793.7
396.4	337.7
217.7	110.7
207.9	80.2
178.3	0.0

Table 2. Data for 16-Ply Composite Panels

16-Ply Cylindrical Projectile	
Initial Velocity (ft/s)	Residual Velocity (ft/s)
590.0	569.6
505.8	467.1
396.5	344.4
304.8	233.6
250.6	172.4
212.7	81.5
206.5	82.2
199.8	83.2
194.6	85.7
191.4	66.2
186.9	36.7

16-Ply Spherical Projectile	
Initial Velocity (ft/s)	Residual Velocity (ft/s)
712.5	634.9
499.9	412.7
398.0	281.3
353.6	210.1
337.0	185.0
320.0	164.0
301.1	81.4
290.5	0.0
286.7	0.0
284.6	0.0

Table 3. Data for 32-Ply Composite Panels

32-Ply Cylindrical Projectiles	
Initial Velocity (ft/s)	Residual Velocity (ft/s)
493.7	410.8
447.2	359.0
373.8	262.2
347.5	208.3
319.4	182.2
301.1	134.6
284.7	82.9
279.7	84.1
268.3	0.0

32-Ply Spherical Projectiles	
Initial Velocity (ft/s)	Residual Velocity (ft/s)
733.3	535.0
673.1	464.7
611.3	385.0
574.7	333.3
539.4	265.4
517.2	223.8
503.9	210.4
492.1	160.6
490.9	201.3
490.3	168.8
482.6	112.2
480.6	44.0
479.8	178.1
478.7	150.5
470.1	141.4
468.4	170.3
457.2	0.0
455.6	0.0

4.3.4 Damage Characterization.

Qualitatively, the damage in the composite panels did not change much from impact to impact. Figure 10 shows the damage caused by a cylindrical projectile. Both the front and back sides of the composite panel are shown. The damage on the front side of the panels (the side the projectile enters) was primarily limited to a one-half-inch-diameter circle (the same size as the projectile). Outside the area, directly under the projectile, the front side of the panel appeared to be completely undamaged with the exception of a few small cracks running parallel to the fibers on the outermost ply. As opposed to the front side, the damage on the back side expands far beyond the area under the projectile. Significant delamination of the final ply was observed on all shots where the projectile penetrated the panel. The delamination typically stretched to the corners of the panel.

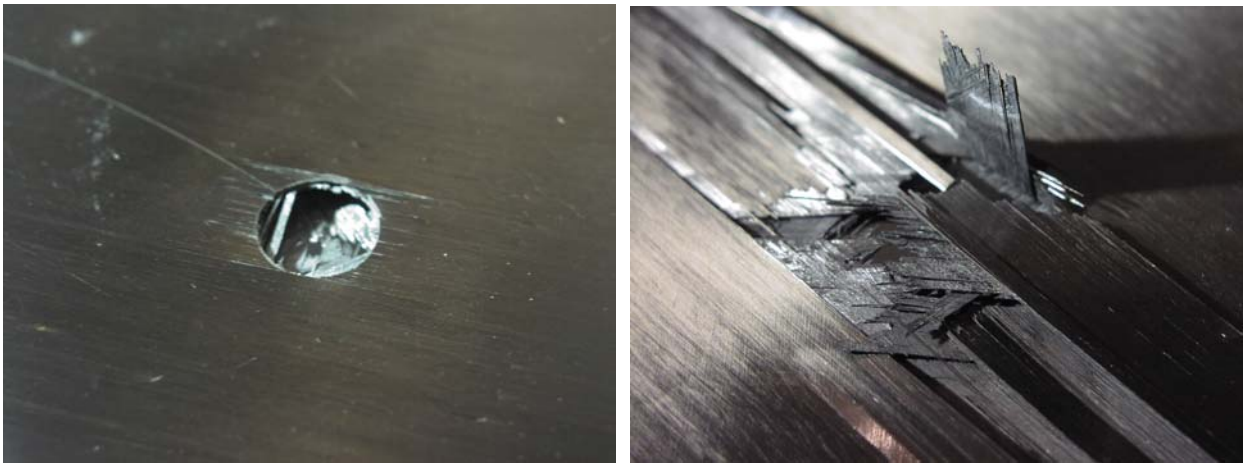

Figure 10. Damage in Composite Panel Caused by Cylindrical Projectile
(Left: Entrance Hole, Right: Exit Hole)

The holes created by cylindrical projectile were very clean. The corners of the cylinder should produce singularities in the stress field all around the edges of the projectile. As a result, the cylinder cut the composite panel like a cookie cutter and, for the thin panels, often pushed a circular plug out the back. The spheres, on the other hand, do not have the sharp corners to cut their way through. The stresses at the point where the sphere first impacted the panel would be high, but nothing compared to the corners of the cylinder. Instead, the holes created by the spheres had no clean edges and were filled with split fibers. The differences are clearly shown in figures 10 and 11. Figure 11 shows the damage resulting from the impact of a spherical projectile. While the entrance holes show a clear distinction, the exit holes remain much the same regardless of the shape of the projectile.

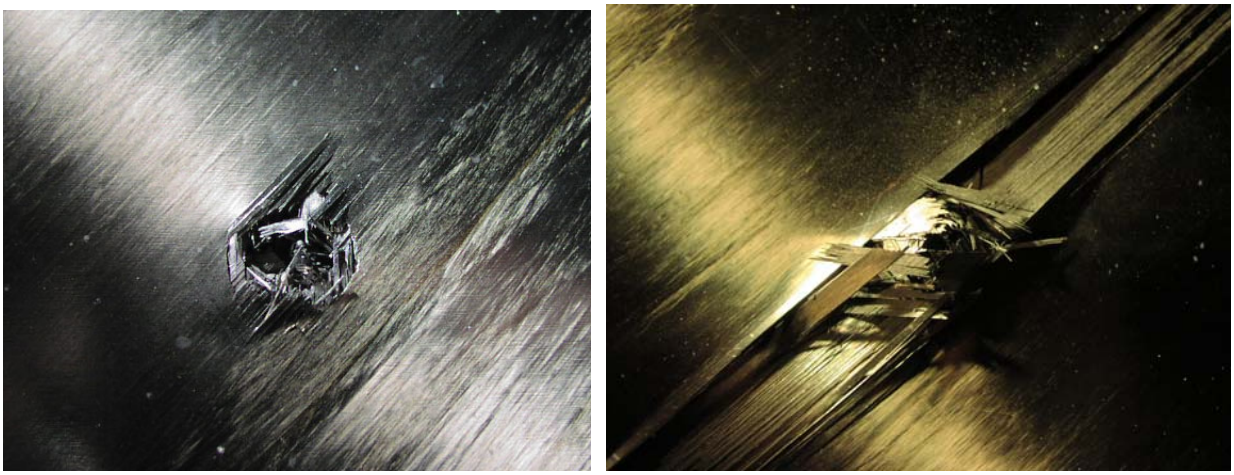

Figure 11. Damage in Composite Panel Caused by Spherical Projectile
(Left: Entrance Hole, Right: Exit Hole)

4.3.5 Composite During Impact.

Figures 12 and 13 show a series of still images taken from the high-speed video of the projectiles impacting the composite sheet. Figure 12 shows a cylindrical projectile impacting the composite panel, and figure 13 shows the impact of a spherical projectile. The projectiles in both figures are moving from right to left. The large black bars on the right are the target mount and holder separated by a spacer to keep the panel perpendicular to the projectile's path.

Figure 12. Cylinder Impacting Composite Panel

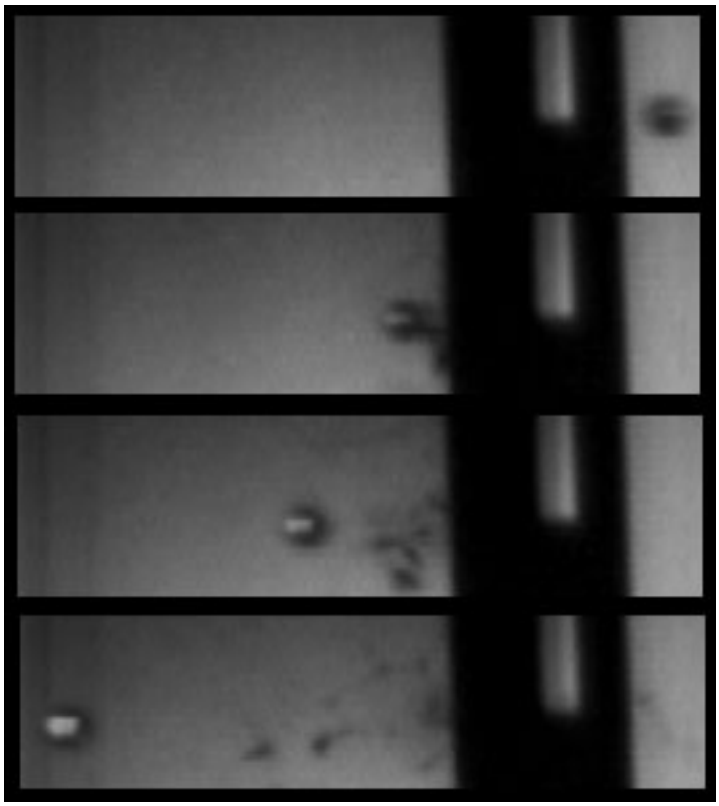

Figure 13. Sphere Impacting Composite Panel

The impact of the cylinder caused significant delamination of the final ply. The large fiber strips that were torn free are clearly shown in figure 12. A small plug the cylinder punched out is also clearly shown in the last frame, directly to the left of the projectile. Unlike the cylindrical projectile, the spherical projectile, shown in figure 13, produced no plug but produced a larger amount of shattering in the panel.

5. ERROR ANALYSIS.

Measurements of the initial and residual velocities of the projectiles were made during every test. There are a number of sources for potential error in these measurements, which will be discussed in the following sections.

5.1 INITIAL VELOCITY.

The initial velocity was measured as the projectile crossed the paths of two lasers. Velocity was determined by the following equation:

$$v = d/t$$

where v is the projectile's initial velocity, d is the distance between the two lasers, and t is the time needed to cross the distance between the two lasers. The error in the velocity as a function of the error in the distance and time measurements is

$$\left(\frac{\delta v}{v}\right)^2 = \left(\frac{\delta d}{d}\right)^2 + \left(\frac{\delta t}{t}\right)^2$$

where δv is the error in the projectile's initial velocity, δd is the error in distance between the two lasers, and δt is the error in the time measurement. The error in the distance measurement can be determined by the tolerance in the milling machine at the University of California, which was used to drill the holes in the photodiode.

Thus

$$d = \frac{2.5}{12} \pm \frac{0.00025}{12} \text{ ft with } \delta d = \frac{0.00025}{12} \text{ ft}$$

The time measured on the Hewlett Packard 53131A Universal Counter differed from shot to shot, but was always larger than 200 microseconds.

The tolerance from the counter was $\delta t = 2.5 \times 10^{-10}$.

This makes

$$\left(\frac{\delta t}{t}\right)^2 \leq 1.5625 \times 10^{-12}$$

Thus

$$\left(\frac{\delta d}{d}\right)^2 = 1 \times 10^{-8}$$

dominates the error in the initial velocity calculation and

$$\left(\frac{\delta v}{v}\right)^2 \approx \left(\frac{\delta d}{d}\right)^2$$

Using this, the error in the initial velocity can be determined to be $\delta v = v \times 10^{-4}$, or a 0.01% error in the initial velocity.

5.2 RESIDUAL VELOCITY.

The residual velocity for each test was determined using a high-speed video camera. Two frames were examined, the position of the projectile was determined for each frame in number of

pixels, and the time between each frame was calculated by the number of frames between the two examined frames. This produced a velocity of pixels per second. To convert this measurement to feet per second, a ruler was placed in the path of the projectile and the number of pixels per feet was determined. Each of these measurements introduced possible sources of error.

$$v = (d/t)$$
$$d = Cx$$

where v is the projectile's initial velocity, d is the distance in feet traveled by the projectile, t is the time between the two frames, x is the distance in pixels, and C is the number of pixels per feet. The error in the velocity as a function of the error in the distance, time, and conversion measurements is

$$\left(\frac{\delta v}{v}\right)^2 = \left(\frac{\delta d}{d}\right)^2 + \left(\frac{\delta t}{t}\right)^2$$

$$\delta d = C\delta x + x\delta C \text{ or } \frac{\delta d}{d} = \frac{\delta x}{x} + \frac{\delta C}{C}$$

where δv is the error in the projectile's initial velocity, δd is the error in the total distance, δx is the error in the pixel distance, δt is the error in the time measurement, and δC is the error in the conversion factor.

C was measured by counting the number of pixels in 6 inches, which was the camera's field of view.

Thus

$$C = \frac{51 \pm 2\,pixels}{0.5\,ft} = 102 \pm 4 \text{ pixels per ft}$$

where $\delta C = 4$.

This error was achieved by assuming the starting and ending pixels could each be off by 1. As the projectile typically traveled half a foot between the initial and final position measurements with an error of 1 pixel for each measurement

$$x = 51 \pm 2 \text{ pixels with } \delta x = 2$$

$$\frac{\delta x}{x} = 0.039 \text{ and } \frac{\delta C}{C} = 0.039\text{, thus } \frac{\delta d}{d} = 0.078$$

The camera took video at a rate of 10,000 frames per second. Thus, $\delta t = 1 \times 10^{-4}$. The projectile traveled a distance of 6 inches. Thus, the total time t depended on the projectile's velocity, or $t = (d / v)$.

Again, the error in the distance measurement dominates and $\delta v = v \times 0.078$, or in other words, there is a 7.8% error in the residual velocity.

5.3 DELAMINATION TESTING.

To aid in the computational modeling of airplane fragment-shielding systems, the mode I interlaminar fracture toughness of unidirectional composite samples of BMS 8-212 was determined at UCB. The results of this work are presented in the UCB report in appendix B. In the experiments, tests were performed on 26-ply samples designed to permit fracture toughness determination according to ASTM D 5528-01. The resistance curves for five delamination samples were determined.

6. SUMMARY.

To calculate the ballistic limit, the scatter in the test data at low velocities made a clear determination difficult to achieve. Instead, the data on the amount of energy absorbed during impact was used. The results at low energies were the most reliable. Only data points where 50% or more of the initial energy was absorbed were used in the calculation. From these values, the average energy absorbed was determined and is shown in table 4. Using these values, the velocity at which 100% of the energy would be absorbed can easily be determined. This represents the velocity at the ballistic limit and is listed in table 5.

Table 4. Energy Absorbed During Impact

	Energy Absorbed (J)	
Projectile:	Sphere	Cylinder
8-Ply	13.5	27.1
16-Ply	31.2	58.3
32-Ply	82.1	124.8

Table 5. Summary of Ballistic Limit Values

	Ballistic Limit (ft/s)	
Projectile:	Sphere	Cylinder
8-Ply	187.1	125.5
16-Ply	284.3	184.0
32-Ply	461.5	269.1

When the number of plies is doubled, the energy absorbed is slightly more than doubled. For the cylindrical projectiles, the increase was approximately 2.15 times. For the spherical projectiles, the increase was closer to 2.5 times. Thus, for the cylindrical projectiles, only a small advantage was gained by increasing the size of the composite panel. The benefit increased when the projectiles were spherically shaped.

The ballistic response of the composite panels depended greatly on the projectile's shape. A cylindrical projectile required almost twice the energy to penetrate the composite, as did a spherical projectile of the same diameter.

7. REFERENCES.

1. Kelly, S. and Johnson, G., "Statistical Testing of Aircraft Materials for Transport Airplane Rotor Burst Shielding," FAA report DOT/FAA/AR-06/9, May 2006.

2. May, C.A., "Small-Scale Ballistic Impact Tests to Optimize Transport Airplane Rotor Burst Fragment Fabric Shielding Designs," FAA report, DOT/FAA/AR-07/43, October 2007.

THE BOEING COMPANY

Table 2.2.2-1 Ply Properties ⑥

TABLE: 2.2.2-1	PLY PROPERTIES
Prepreg Material Specicification:	BMS 8-212, TYPE III CLASS 1 or 3, GRADE 145 or 190
Resin Content:	37 (% WT)
Cured Ply Thickness:	0.0059 (in) - GRADE 145 0.0080 (in) - GRADE 190
Density:	0.056 lb/in^3
Process Specification:	BAC 5317-1

PROPERTY		UNIT	ENVIRONMENTAL CONDITION					
			-75°F		70°F		180°F ⑤	
			DRY	WET	DRY	WET	DRY	WET
MODULUS ②	E_1 ①	Msi	17.1					
	E_2	Msi			1.28			
	G_{12}	Msi	0.82		0.66			0.54
	G_{13}	Msi	0.82		0.66			0.54
	G_{23}	Msi	0.82		0.66			0.54
POISSON'S RATIO	ν_{12}	----	0.34					
COEFFICIENTS OF LINEAR THERMAL EXPANSION ③	α_1	in/in °F	$.02 \times 10^{-6}$				$.02 \times 10^{-6}$	
	α_2	in/in °F	15×10^{-6}				15×10^{-6}	
COEFFECIENTS OF LINEAR MOISTURE EXPANSION ④	β_1	in/in %M						
	β_2	in/in %M						
THERMAL CONDUCTIVITY	κ_1	BTU/(hr ft °F)						
	κ_2	BTU/(hr ft °F)						
	κ_3	BTU/(hr ft °F)						

① E_1 is the average of tension and compression moduli. For special analyses use tension/compression modulus adjustment factors to determine tension or compression E_1.

② Modulus values are secant values at a strain level of 4000 μ in/in. For special analysis use modulus versus strain curves to determine secant values at the desired strain level.

③ Values are for expansion between -75° F and 70° F, and 70° F and 180° F.

④ %M = Percent absorbed moisture by weight.

⑤ 180°F values are to be used for 160°F environment.

DG-100-531

⑥ Approved for public release

APPENDIX B– DELAMINATION TESTING RESULTS

Determination of the Interlaminar Toughness of Unidirectional BMS 8-212 Composites

George C. Johnson
Kevin Donovan
David Kashevaroff

Department of Mechanical Engineering
University of California Berkeley, CA 94720-1740

Abstract

To aid in the computational modeling of airplane fragment-shielding systems, the mode I interlaminar fracture toughness of unidirectional composite samples of BMS 8-212 was determined. This carbon-reinforced composite material has been widely studied by our partners at Boeing, who supplied the material. In the experiments presented here, tests were performed on 26-ply coupons designed to permit fracture toughness determination according to ASTM Standard D5528-01. The resistance curves for five delamination coupons were determined, showing an average steady-state fracture toughness of $G_{Ic} = 126 \pm 14 \ J/m^2$.

Introduction

In order to minimize the possibility that fragments of airplane engine rotors break off in use, penetrate the plane fuselage and damage critical components such as fuel and hydraulic lines, a program to design and analyze potential ballistic shields has been supported by the Federal Aviation Administration. Computational modeling of these shields requires a thorough understanding of the properties of the materials involved. This report provides data for the failure characteristics of unidirectional composite samples of BMS 8-212. Specifically, the mode I interlaminar fracture toughness of this carbon fiber-reinforced polymer matrix composite was determined at relatively low rates of loading, and the ballistic characteristics of this material were examined for two thicknesses and three projectile shapes.

The material tested was a carbon fiber-reinforced polymer matrix composite designated BMS 8-212N, Type III, Class 1, Grade 190. This material has nominal resin content of 37% by weight and a nominal carbon fiber areal weight of 190 g/m^2. All specimens were manually laid up using unidirectional prepreg tape whose thickness is expected to be between 0.19 *mm* and 0.20 *mm*. Specimens used for fracture toughness determination were designed to have a nominal thickness of 5 mm, requiring 26 plies. Specimens used for ballistic testing had nominal thicknesses of 1.59 mm (1/16 in.) and 3.18 mm (1/8 in.), requiring 8 and 16 plies, respectively.

Testing to determine the fracture toughness of this material was performed in accordance with ASTM Standard D5528-01 [1]. Loading was applied using a screw driven machine with two sets of instruments used to obtain the force and crack-opening displacement data – one that provides relatively coarse (machine-level) measurements and one that provides finer (test-level) measurements. Data from the fine-scale load and displacement sensors were then used to calculate the fracture toughness of the composites using the three methods provided in ASTM Standard D5528-01: Modified Beam Theory, Compliance Calibration and Modified Compliance Calibration.

Delamination Testing

The composite samples tested (shown schematically in Figure 1, with nominal sample dimensions given in Table I) were manufactured according to the specifications of ASTM Standard D5528-01, with a thin Teflon film inserted at one end to create an initial crack (of length a_0) in the material. By recording this delamination length, as well as the corresponding load and extension, the fracture toughness was determined using the three methods given in this Standard.

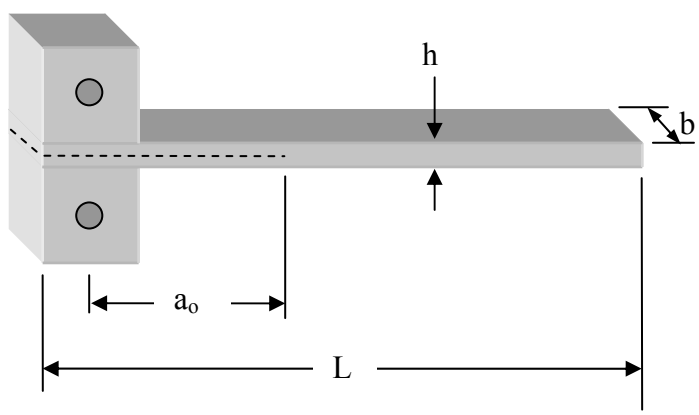

Figure 1. Schematic diagram of the composite samples. The dashed line indicates the location of the initial crack created by inserting a Teflon film between the middle lamina of the composite.

Table I. Nominal dimensions of the samples for delamination testing

Parameter	Dimension (mm)
L	127
b	25.4
a_0	38.1
h*	5

* The average thickness varied substantially among the different samples tested, ranging from 4.86 *mm* to 5.91 *mm*. There was also some variation along the length of each sample.

Delamination Analysis

ASTM Standard D5528-01 [1] provides three methods for determining the critical toughness for mode I interlaminar fracture (G_{Ic}) of unidirectional composites from measurements of the crack opening displacement δ, the applied loading P and the crack length a. A schematic diagram of the loaded sample showing these parameters is given in Figure 2, where the loading blocks are not shown.

The simplest approach treats the composite sample as a double cantilever beam, with each beam originating at the origin of the crack, leading to the expression for fracture toughness

$$G_{Ic}^{B} = \frac{3P\delta}{2ba}. \tag{1}$$

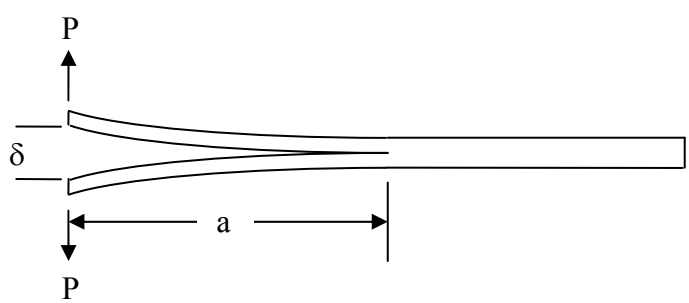

Figure 2. Schematic diagram of the composite sample under loading (from Figure 3 of [1]).

ASTM Standard D5528-01 warns that this method generally overestimates G_{Ic} because the specimen may rotate at the crack tip and because the location of the crack tip may be difficult to determine accurately. To correct for this, a modified approach is given that treats the double cantilever beam as if the actual crack length is slightly longer than the observed length a. Thus, a

in Eq. (1) is replaced by, $a + |\Delta|$, where Δ is determined from the experimental data under the assumption that the beam compliance C,

$$C = \delta/P, \tag{2}$$

should vary as the cube of the crack length. Thus, a plot of the cube root of compliance, determined from the measured crack opening displacement and force, versus the observed delamination length should be a straight line whose intercept is Δ. Figure 3 shows this graphically for simulated data. The corrected expression for the fracture toughness using this approach, referred to as the "modified beam theory" or MBT, is then

$$G_{Ic}^{MBT} = \frac{3P\delta}{2b(a+|\Delta|)}. \tag{3}$$

The second method for determining the fracture toughness is referred to as the compliance calibration (CC) method. Instead of the factor of three in the numerator for the determination of G_{Ic}, which reflects the assumed cubic relation between compliance and crack length, the CC method uses the apparent power law dependence between C and the crack length a, as in

$$C = \alpha a^n. \tag{4}$$

The power n, is identified as the slope of the least-squares best fit line to a log-log a plot of C vs. a, as shown schematically in Figure 4. The fracture toughness using this method is then

$$G_{Ic}^{CC} = \frac{nP\delta}{2ba} \tag{5}$$

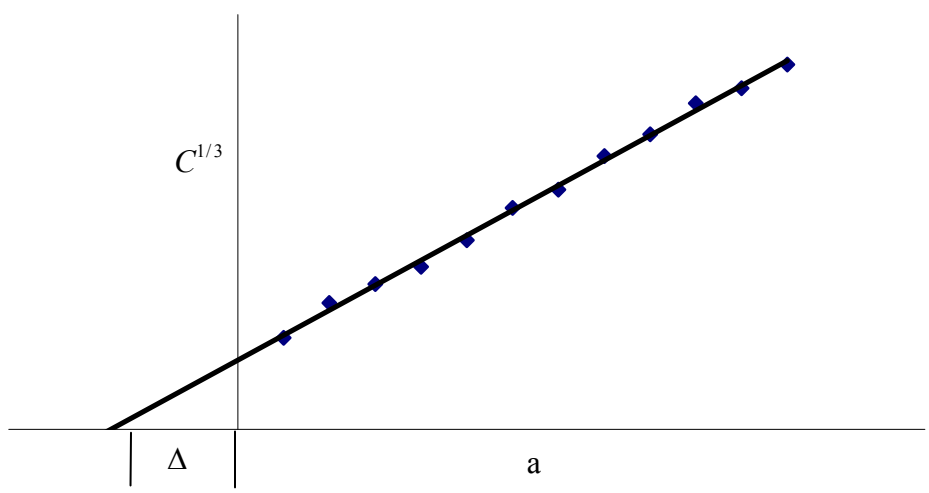

Figure 3. Plot of the cube root of the compliance vs. crack length from which the crack length correction, Δ, is determined (from Figure 4 of [1]).

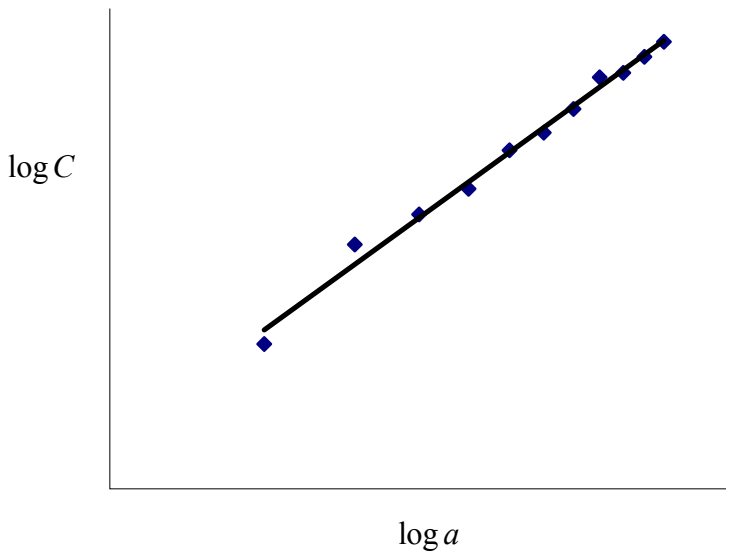

Figure 4. Compliance calibration

The final method provided in ASTM Standard D5528-01 [1] is referred to as the modified compliance calibration (MCC) method. This method eliminates the use of the crack length a in the direct calculation of the fracture toughness through an identification of a parameter similar to α in Eq. (4). Specifically, the MCC method identifies the parameter A_1 appearing in the expression

$$\frac{a}{h} = A_1 C^{1/3} . \tag{6}$$

This new parameter is determined from a plot of the crack length vs. the cube root of the experimentally determined compliance. The fracture toughness using this method is then

$$G_{Ic}^{MCC} = \frac{3P^2 C^{2/3}}{2A_1 bh} . \tag{7}$$

Note that Eq. (7) does not involve the (difficult to measure) crack length directly at each data point. Instead, G_{Ic}^{MCC} is determined through measurements of the force and the crack opening displacement once the parameter A_1 is known. It is also worth noting that although the sample thickness h appears explicitly in Eq. (7), its presence in Eq. (6) defining A_1 essentially removes its influence in the final toughness calculation.

Delamination Testing Procedures

The fine-scale extensometer was calibrated by attaching it to a micrometer and recording the change in output voltage for known positions changes of the micrometer. The test-level load cell was calibrated using weights hung directly from the load cell.

The composite specimens were fabricated at Boeing to nominal dimensions provided in Table I. Before testing each specimen, loading blocks were attached to the end of the specimen, and the location of the initial crack tip was identified and marked. Following the testing procedure outlined in ASTM Standard 5528-01, the edge of each specimen was marked every millimeter beyond the initial crack location for the first 15 *mm*, then it was marked every 5 millimeters for a distance up to 40 *mm* from the initial crack tip. A side-view schematic of the specimen prior to testing is shown in Figure 5.

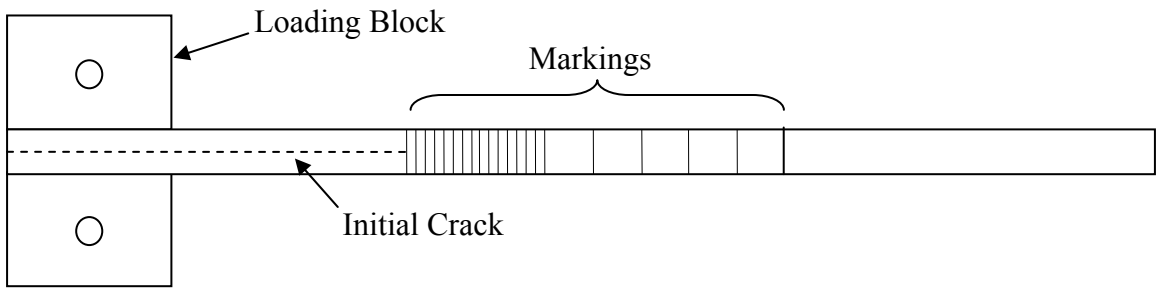

Figure 5. Side view of a prepared sample. Markings are spaced 1 *mm* apart until the 15th millimeter. After that, they are spaced 5 *mm* apart.

Tests were run at loading rates of 0.5 *mm/min*, 1.0 *mm/min* and 5.0 *mm/min*. A variety of techniques were used to monitor the location of the crack tip during the process of loading. Visual observation of the crack tip with the aid of a magnifying glass to enhance the clarity of the process zone was found to be challenging at the higher rate tests. A standard analog video camera and a high-speed (Phantom 4) digital video camera were also used for various tests.

In each case, the object was to quantitatively determine the crack tip location as a function of time so that an association of a could be made with the applied load P and crack opening displacement δ at corresponding times. The latter two measurements were made with data-logging hardware and software.

Delamination Results and Discussion

Calibration data for the test-level extensometer and load cell are shown in Figures 6 and 7, respectively. In each case, changes in the output voltage vary linearly with changes in the relevant measurand. The equation for the linear least squares fit for each curve is given, where it

is worth noting that the measurand data are in English units (inches and pounds). All physical values were converted to SI (meters and Newtons) before calculations were performed.

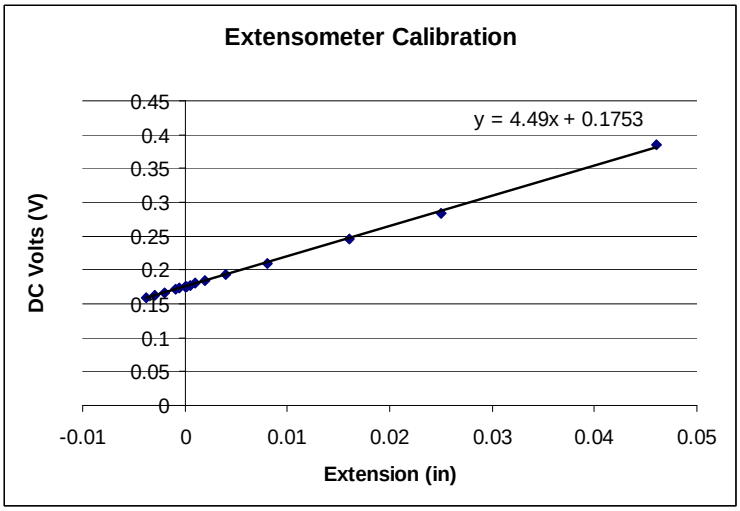

Figure 6. Extensometer calibration

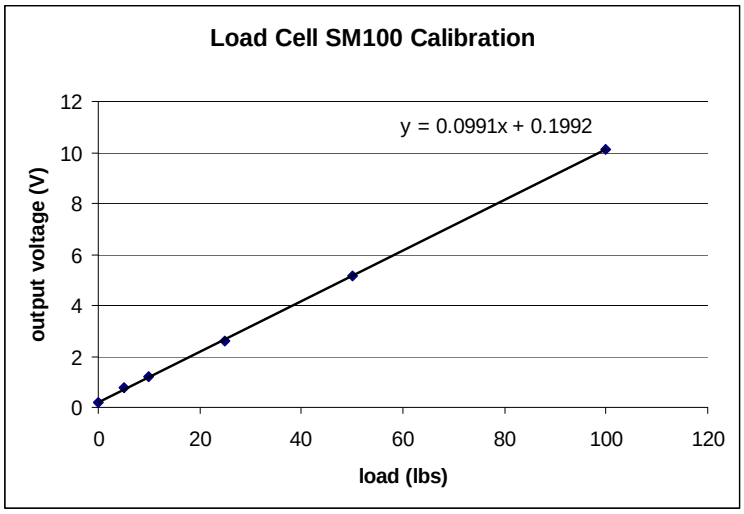

Figure 7. Load cell calibration

A typical load vs. crack opening displacement curve is shown in Figure 8, with the corresponding crack length vs. crack opening displacement data shown in Figure 9. Figure 9 also shows the relevant load data, which appears smoother than in Figure 8 because of the limited number of data points available for the crack length. The particular sample shown in these plots was loaded at 1.0 *mm/min*, and is identified as "Sample 4."

Prior to propagation of the crack, the stiffness (inverse of the compliance) is essentially constant at 87 *N/mm*, reflected by the linear relationship between P and δ. The load peaks at 114 *N*, corresponding to a crack opening displacement of 1.3 *mm*. The crack then advances rapidly from a = 38 *mm* to a = 48 *mm*. Just before the crack advances, the specimen is in an "over-

driven" state, which occurs since the initial crack is not ideally sharp. During this initial crack advance, the load drops abruptly to 54 *N*, then rises slowly with increasing crack opening, reaching a second, much smaller, peak of 63 *N* at δ = 1.64 *mm*. Steady crack advance is observed after a crack opening displacement of around 2 *mm*, and a crack length of around 53 *mm*.

The measured crack opening displacement δ, crack length *a*, and applied load *P* are given in Table II, along with the calculated compliance *C* and each of the three estimates of fracture toughness, G_{Ic}^{MBT}, G_{Ic}^{CC} and G_{Ic}^{MCC}. These estimates of G_{Ic} are plotted against crack length in Figure 10. Examination of the fracture toughness results show that three techniques are quite consistent with each other throughout the test. This agreement between methods is similar to that reported in ASTM Standard 5528-01.

The results shown in Table II and Figure 10 are typical for all tests that provided useful data. The resistance (or R-curve) rises after the initial crack advance, reaching a plateau at a crack length of about 53 *mm* (corresponding to a crack advance of 15 *mm*).

The experimentally determined R-curves for five specimens, loaded at rates of 0.5 *mm/min*, 1.0 *mm/min* and 5.0 *mm/min*, are shown in Figure 11. For each test, there was excellent agreement between the three fracture toughness estimates, comparable to that observed for Sample 4. Thus, the results shown in Figure 11 are for the average of these three values at each data point. At rates below 1 *mm/min*, it was possible to determine the crack location directly, with aid of a magnifying glass, or with a standard video camera. For the higher rate, a high speed digital camera was used.

While each of the curves follows the same basic trend, there are too few tests at each loading rate to determine whether there is any rate sensitivity for the fracture toughness. Assuming none, and considering the values at crack lengths of δ = 58 *mm* and beyond, suggests an average overall fracture toughness of $G_{Ic} = 126 \pm 14 \ J/m^2$, where the uncertainty is given as one standard deviation.

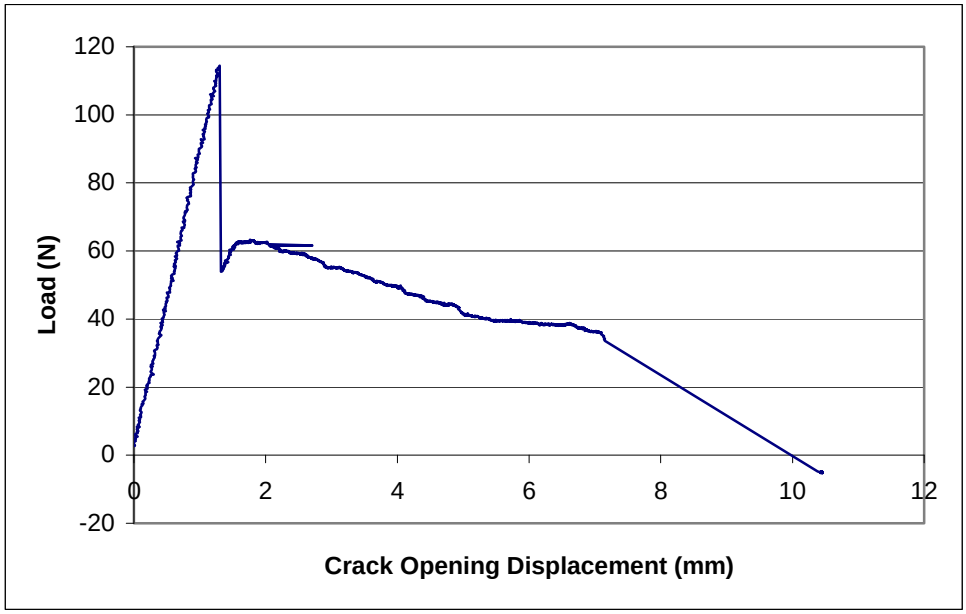

Figure 8. Applied load P versus crack opening displacement δ for sample 4, loaded at 1 *mm/min*.

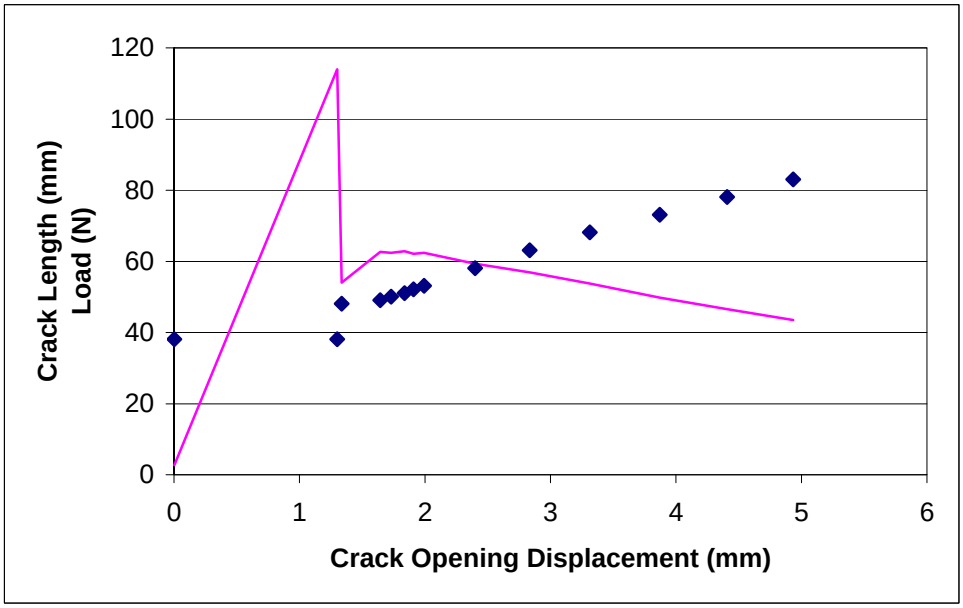

Figure 9. Crack length a (diamonds) and applied load P (solid line) vs. crack opening displacement δ for sample 4, loaded at 1 *mm/min*.

Table 2. Measured and calculated quantities for sample 4, loaded at 1 *mm/min*. Additional parameters for the fracture toughness calculations are derived from all data shown, with the parameters themselves given in footnotes.

Crack Opening	Crack Length	Load	Compliance	G_{Ic}^{MBT} [1]	G_{Ic}^{CC} [2]	G_{Ic}^{MCC} [3]
δ *(mm)*	*a* (*mm*)	*P (N)*	*C (mm/N)*		(J/m^2)	
1.64	49	62.7	0.0262	113	114	112
1.73	50	62.4	0.0277	116	117	115
1.84	51	62.2	0.0292	122	123	121
1.91	52	62.1	0.0307	123	124	122
1.99	53	62.4	0.0319	127	127	127
2.40	58	59.3	0.0405	133	133	134
2.84	63	56.9	0.0499	140	139	141
3.31	68	53.7	0.0617	144	142	145
3.87	73	49.8	0.0777	146	143	146
4.41	78	46.6	0.0946	146	143	145
4.93	83	43.5	0.113	144	140	143

[1] Additional parameter for Modified Beam Theory: $\Delta = 5$ *mm*
[2] Additional parameter for Compliance Calibration: $n = 2.75$
[3] Additional parameter for Modified Compliance Calibration: $A_1 h = 1.83 N^{1/3} m^{2/3}$

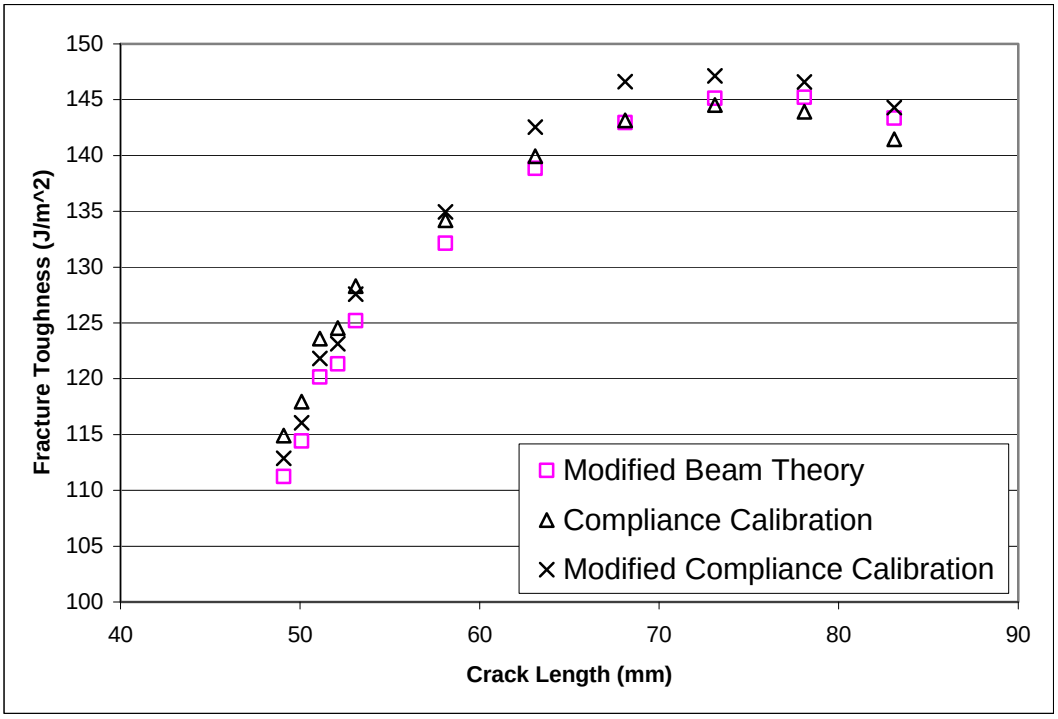

Figure 10. Fracture toughness values (in J/m^2) for Sample 4, loaded at 1 *mm/min*

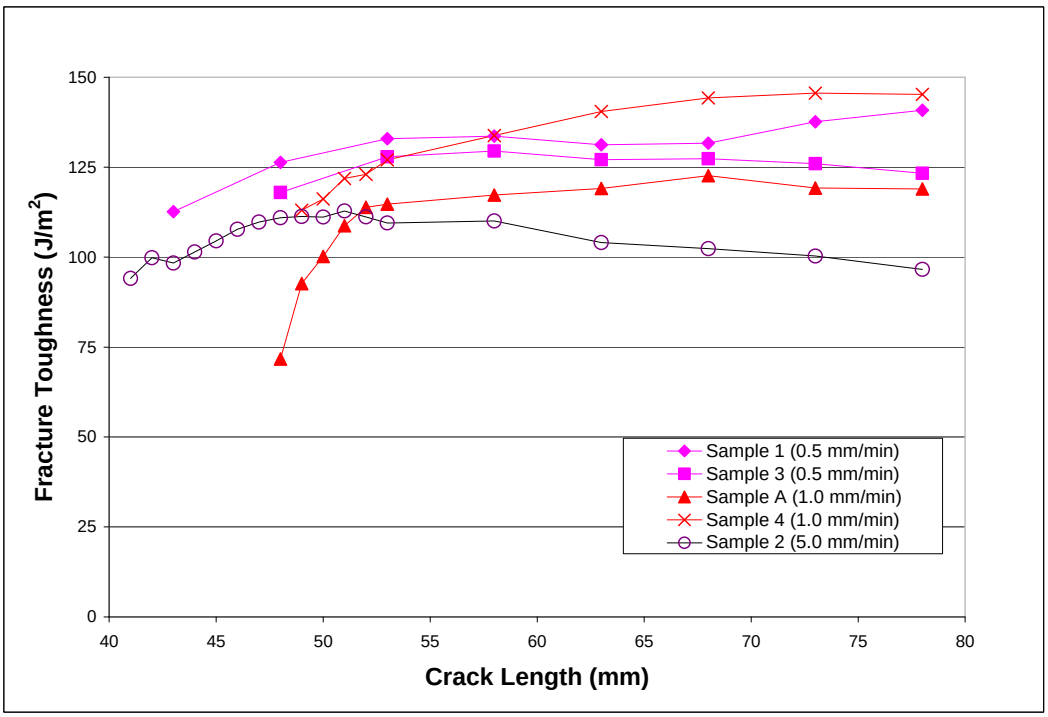

Figure 11. Fracture toughness for five specimens loaded at rates of 0.5, 1.0 and 5.0 *mm/min*. Values shown are averages of G_{Ic}^{MBT}, G_{Ic}^{CC} and G_{Ic}^{MCC} at each data point.

As noted in Table I, there is substantial variation in thickness among the samples, which is magnified when considering the influence on sample stiffness or compliance since the stiffness varies as the cube of the thickness. This large variation in initial stiffness is indeed observed between the different samples, as shown in Figure 12. The initial stiffness of the thickest sample tested is over twice that of the thinnest sample. However, the fracture toughness results are not sensitive to sample thickness as there is no correlation seen in Figure 11 between sample thickness and fracture toughness.

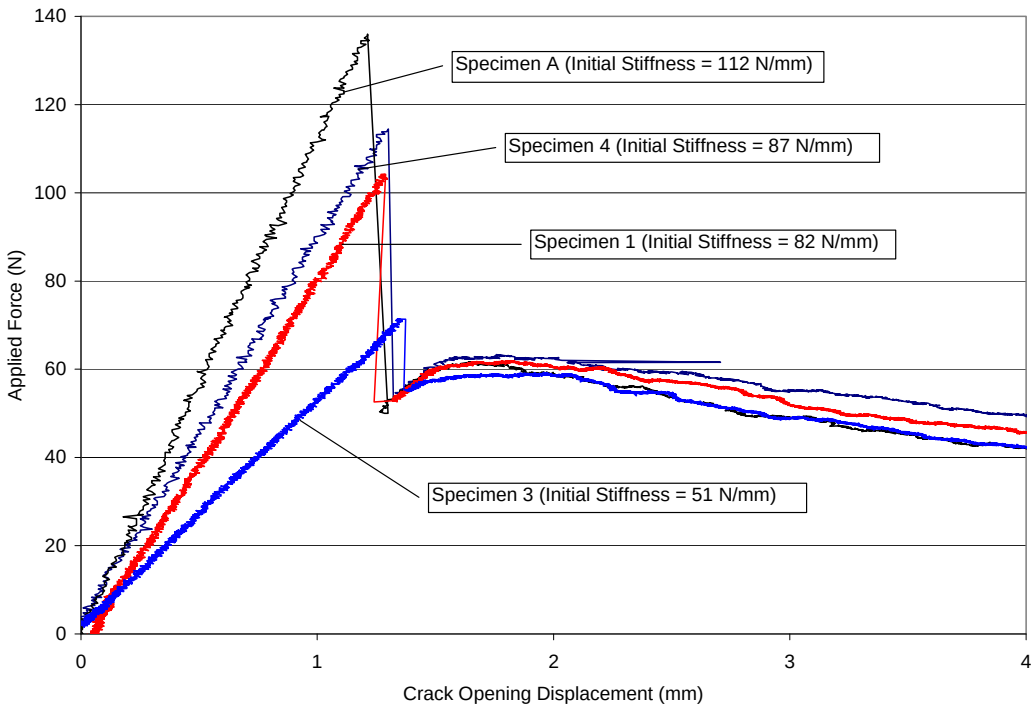

Figure 12. Force vs. crack opening displacement for four samples, illustrating the substantial variation in initial stiffness caused by variations in sample thickness. The load curve is much less sensitive once the crack begins to grow.

References

[1] *Standard Test Method for Mode 1 Interlaminar Fracture Toughness of Unidirectional Fiber-Reinforced Polymer Matrix Composites*, ASTM International